International Journal of Mechanical System Dynamics

WILEY

IJMSD International Journal of Mechanical System Dynamics Open Access

RESEARCH ARTICLE OPEN ACCESS

NExT-LF: A Novel Operational Modal Analysis Method via Tangential Interpolation

Gabriele Dessena[1] | Marco Civera[2] | Ali Yousefi[2] | Cecilia Surace[2]

[1]Department of Aerospace Engineering, Universidad Carlos III de Madrid, Leganés, Madrid, Spain | [2]Department of Structural, Geotechnical and Building Engineering, Politecnico di Torino, Turin, Italy

Correspondence: Marco Civera (marco.civera@polito.it)

Received: 12 December 2024 | **Revised:** 26 February 2025 | **Accepted:** 4 March 2025

Funding: The first author has been supported by the Madrid Government (Comunidad de Madrid—Spain) under the Multiannual Agreement with the Universidad Carlos III de Madrid (UC3M) (IA_aCTRl-CM-UC3M) and by the Grants for research activity of young PhD holders, part of the UC3M Own Research Program (Ayudas para la Actividad Investigadora de los Jóvenes Doctores, del Programa Propio de Investigación de la UC3M). The second author is supported by the Centro Nazionale per la Mobilità Sostenibile (MOST—Sustainable Mobility Center), Spoke 7 (Cooperative Connected and Automated Mobility and Smart Infrastructures), Work Package 4 (Resilience of Networks, Structural Health Monitoring and Asset Management).

Keywords: Loewner Framework | noise resilient techniques | operational modal analysis | tangential interpolation

ABSTRACT

Operational modal analysis (OMA) is vital for identifying modal parameters under real-world conditions, yet existing methods often face challenges with noise sensitivity and stability. This study introduces NExT-LF, a novel method that combines the well-known Natural Excitation Technique (NExT) with the Loewner Framework (LF). NExT enables the extraction of Impulse Response Functions from output-only vibration data, which are then converted into the frequency domain and used by LF to estimate modal parameters. The proposed method is validated through numerical and experimental case studies. In the numerical study of a two-dimensional Euler–Bernoulli cantilever beam, NExT-LF provides results consistent with analytical solutions and those from standard methods, NExT with Eigensystem Realization Algorithm (NExT-ERA) and stochastic subspace identification with canonical variate analysis. Additionally, NExT-LF demonstrates superior noise robustness, reliably identifying stable modes across various noise levels where NExT-ERA fails. Experimental validation on the Sheraton Universal Hotel is the first OMA application to this structure, confirming NExT-LF as a robust and efficient method for output-only modal parameter identification.

1 | Introduction

The importance of modal analysis in modern engineering is undisputed. Modal parameters—namely, natural frequencies (ω_n), damping ratios (ζ_n), and mode shapes ($\boldsymbol{\phi}_n$)—are used for a variety of tasks across various engineering systems, such as aircraft wings [1], fuel pumps [2], and civil structures [3]. Nevertheless, this characterization is not carried out for its own sake but to inform the design process, such as in aircraft certification [4], updating existing finite element models [5], and/or for structural health monitoring (SHM) [6, 7]. In particular, modal analysis has been used to monitor the health of infrastructure such as railway bridges [8] and tall buildings [9] while also revealing the effect of complex fluid-structure interactions on system dynamics, such as those in conical shells partially filled with fluids [10]. Advanced techniques have also enabled dynamic parameter identification in robotic systems, overcoming nonlinearities to enhance their control precision [11].

In general, there are two main approaches for modal analysis: experimental modal analysis (EMA) and operational modal analysis (OMA). EMA relies on controlled excitations to characterize structure dynamics accurately. Due to the requirement of a controlled environment, EMA is resource-intensive and constrained by the need for specialized setups, making it unsuitable for many large-scale or in situ applications [12]. By contrast, OMA exploits

---

ambient vibrations, eliminating the need for external input forces, such as those generated by shaker tables [13]. This makes OMA particularly advantageous for scenarios, such as monitoring long-span bridges [14], evaluating aerospace systems during operation [15], and assessing historic buildings [16].

Central to EMA and OMA is system identification (SI), here defined as the process of extracting dynamic properties and/or models from measured data [17]. SI techniques generally fall into two categories: time-domain and frequency-domain methods. Within these, input–output approaches, as used in EMA, rely on known external excitations to establish dynamic relationships (such as frequency response functions—FRFs). Conversely, output-only techniques, such as those employed in OMA, can use stochastic ambient excitations, by modeling them as random processes [18]. Recent advances in SI, including artificial intelligence and machine learning techniques, have streamlined key processes, such as interpreting stabilization diagrams or denoising. However, while these innovations improve automation and accuracy, they often introduce computational complexity and may require higher data quality [19].

Moreover, new modal identification techniques, as well as improved variants of existing algorithms, have been recently introduced to address the noise robustness and mode consistency problem. In particular, a robust implementation of the stochastic subspace identification (SSI) covariance-driven variant has been proposed in Reference [20] to incorporate a probabilistic method to reduce the risk of misidentifying outliers as physical modes. Furthermore, a dual unscented Kalman filter approach to simultaneously evaluate changes to the mass distribution and kinematic state of an in-orbit satellite flexible dynamics has been introduced in Reference [21], and a Bayesian approach for the OMA of systems having closely spaced modes has been presented in Reference [22] and applied to an existing suspension footbridge. Notably, a single-input multi-output (SIMO) identification method widely applied in electrical engineering [23], the Fast Relaxed Vector Fitting, has been successfully applied in modal identification and vibration-based SHM to exploit its computational efficiency [24].

In this wave of emerging SI techniques, the Loewner Framework (LF) [25], also coming from electrical engineering [26], has distinguished itself as a powerful tool for SIMO SI, offering strong noise resilience and high accuracy in modal parameter estimation. However, these have not yet been proven in an OMA (unknown input) setting. Nevertheless, the Natural Excitation Technique (NExT) [27] has demonstrated significant capability in output-only applications, effectively allowing the use of ambient vibrations with input–output modal identification methods [28]. These two methods, although historically separate, present complementary strengths. Hence, this study introduces a novel combination of these techniques, referred to as the NExT-LF approach, to tackle OMA. By combining the computational simplicity of NExT with the noise rejection capabilities of the LF, the proposed method strives to address the limitations, in existing techniques (such as NExT-ERA) of noise sensitivity. Hence, the pairing of NExT and the Eigensystem Realization Algorithm (ERA) [29], NExT-ERA [30], is used as a benchmark method in this study, alongside—for the numerical system only—the well-known SSI with Canonical Variate Analysis [31]. Thus, the main contributions of this study are as follows:

- The development of the NExT-LF method, integrating the LF with NExT, to achieve OMA capability.
- Numerical validation of NExT-LF, across varying noise conditions on a numerical system.
- Experimental validation of the method on a first-in-literature identified structure: The Sheraton Universal Hotel in Universal City, North Hollywood, California (USA).

To achieve its aims, this study tackles the following:

1. In Section 2 (Methodology), the LF identification method is introduced, before discussing the output-only enabling method, NExT, and their pairing.
2. In Section 3 (Numerical Case Study), the proposed method is applied to a numerical of a cantilever beam to preliminarily assess its noise robustness characteristics.
3. In Section 4 (OMA of the Sheraton Universal Hotel), the Sheraton Universal Hotel environmental vibration is analyzed, and the modal parameters are extracted via NExT-LF and NExT-ERA.
4. The conclusions (Section 5) end this paper.

2 | Methodology

2.1 | Loewner Framework

Previously, the LF algorithm has been employed for the modeling of a multiport electrical system [26] and utilized for aerodynamic model order reduction in the context of aeroservoelastic modeling [32]. Later, the first and second authors applied the LF for the identification of modal parameters from SIMO mechanical systems in Reference [25], verified its computational efficiency in Reference [33], and later assessed its robustness to noise for SHM in Reference [34]. Further developments have been carried out for the extension of the LF for the extraction of modal parameters from multi-input multi-output systems in References [35, 36], but the version considered in this study is the SIMO version first introduced in Reference [25].

Let us begin by defining the Loewner matrix $\mathbb{L}$: Given a row array of pairs of complex numbers (μ_j, v_j), $j = 1, \ldots, q$, and a column array of pairs of complex numbers (λ_i, w_j), $i = 1, \ldots, k$, with λ_i, μ_j distinct, the associated $\mathbb{L}$, or divided-differences matrix is

$$\mathbb{L} = \begin{bmatrix} \frac{\boldsymbol{v}_1 - \boldsymbol{w}_1}{\mu_1 - \lambda_1} & \cdots & \frac{\boldsymbol{v}_1 - \boldsymbol{w}_k}{\mu_1 - \lambda_k} \\ \vdots & \ddots & \vdots \\ \frac{\boldsymbol{v}_q - \boldsymbol{w}_1}{\mu_q - \lambda_1} & \cdots & \frac{\boldsymbol{v}_q - \boldsymbol{w}_k}{\mu_q - \lambda_k} \end{bmatrix} \in \mathbb{C}^{q \times k}. \tag{1}$$

If there is a known underlying function ϕ, then $\boldsymbol{w}_i = \phi(\lambda_i)$ and $\boldsymbol{v}_j = \phi(\mu_j)$.

Löwner established a relationship between $\mathbb{L}$ and rational interpolation, often referred to as Cauchy interpolation [37]. This connection enables the definition of interpolants through the determinants of submatrices of $\mathbb{L}$. As shown in References [38, 39], rational interpolants can be obtained directly from $\mathbb{L}$. This study adopts the approach based on the Loewner pencil, which comprises the $\mathbb{L}$ and $\mathbb{L}_{\mathrm{s}}$ matrices. Here, $\mathbb{L}_{\mathrm{s}}$ represents the *shifted Loewner matrix*, a concept to be defined later.

To describe the working principle of the LF, consider a linear time-invariant dynamical system $\boldsymbol{\Sigma}$ characterized by m inputs, p outputs, and k internal variables, represented in descriptor form as

$$\boldsymbol{\Sigma} : \boldsymbol{E}\frac{\mathrm{d}}{\mathrm{d}t}\boldsymbol{x}(t) = \boldsymbol{A}\boldsymbol{x}(t) + \boldsymbol{B}\boldsymbol{u}(t), \quad \boldsymbol{y}(t) = \boldsymbol{C}\boldsymbol{x}(t) + \boldsymbol{D}\boldsymbol{u}(t), \tag{2}$$

where $\boldsymbol{x}(t) : \in: \mathbb{R}^k$ represents the internal variable, $\boldsymbol{u}(t) : \in: \mathbb{R}^m$ denotes the input function, and $\boldsymbol{y}(t) : \in: \mathbb{R}^p$ corresponds to the output. The constant system matrices are

$$\boldsymbol{E}, \boldsymbol{A} \in \mathbb{R}^{k\times k}, \boldsymbol{B} \in \mathbb{R}^{k\times m}, \boldsymbol{C} \in \mathbb{R}^{p\times k}, \boldsymbol{D} \in \mathbb{R}^{p\times m}. \tag{3}$$

The Laplace transfer function, $\boldsymbol{H}(s)$, of $\boldsymbol{\Sigma}$ can be expressed as a $p \times m$ rational matrix function, provided that the matrix $\boldsymbol{A} - \lambda\boldsymbol{E}$ is nonsingular for a given finite value λ, where $\lambda \in \mathbb{C}$:

$$\boldsymbol{H}(s) = \boldsymbol{C}(s\boldsymbol{E} - \boldsymbol{A})^{-1}\boldsymbol{B} + \boldsymbol{D}. \tag{4}$$

Let us examine the general framework of tangential interpolation, commonly identified as rational interpolation along tangential directions [40]. The associated right interpolation data are expressed as follows:

$$\left.\begin{aligned} &(\lambda_i; \boldsymbol{r}_i, \boldsymbol{w}_i), \quad i = 1, \ldots, \rho, \\ \boldsymbol{\Lambda} &= \operatorname{diag}\left[\lambda_1, \ldots, \lambda_k\right] \in \mathbb{C}^{\rho\times\rho}, \\ \boldsymbol{R} &= \left[\boldsymbol{r}_1 \cdots \boldsymbol{r}_k\right] \in \mathbb{C}^{m\times\rho}, \\ \boldsymbol{W} &= \left[\boldsymbol{w}_1 \cdots \boldsymbol{w}_{\mathbf{k}}\right] \in \mathbb{C}^{\rho\times\rho}. \end{aligned}\right\} \tag{5}$$

Similarly, the left interpolation data are defined as follows:

$$\left.\begin{aligned} &(\mu_j, \boldsymbol{l}_j, \boldsymbol{v}_j), \quad j = 1, \ldots, \nu, \\ \boldsymbol{M} &= \operatorname{diag}\left[\mu_1, \ldots, \mu_q\right] \in \mathbb{C}^{\nu\times\nu}, \\ \boldsymbol{L}^{\mathrm{T}} &= \left[\boldsymbol{l}_1 \cdots \boldsymbol{l}_\nu\right] \in \mathbb{C}^{p\times\nu}, \\ \boldsymbol{V}^{\mathrm{T}} &= \left[\boldsymbol{v}_1 \cdots \boldsymbol{v}_q\right] \in \mathbb{C}^{m\times\nu}. \end{aligned}\right\} \tag{6}$$

The values λ_i and μ_j correspond to the points at which $\boldsymbol{H}(s)$ is evaluated, representing the frequency bins in this context. The vectors $\boldsymbol{r}_i$ and $\boldsymbol{l}_j$ denote the right and left tangential general directions, which are typically chosen randomly in practice [32], while $\boldsymbol{w}_i$ and $\boldsymbol{v}_j$ represent the respective tangential data. Establishing a connection between $\boldsymbol{w}_i$ and $\boldsymbol{v}_j$ and the transfer function $\boldsymbol{H}$, linked to the realization $\boldsymbol{\Sigma}$ in Equation (2), resolves the rational interpolation problem:

$$\begin{aligned} &\boldsymbol{H}(\lambda_i)\boldsymbol{r}_i = \boldsymbol{w}_i, j = 1, \ldots, \rho \\ &\text{and} \\ &\boldsymbol{l}_i\boldsymbol{H}(\mu_j) = \boldsymbol{v}_j, i = 1, \ldots, \nu \end{aligned} \tag{7}$$

ensuring that the Loewner pencil satisfies Equation (7). Next, consider a set of points $Z = z_1, \ldots, z_N$ in the complex plane and a rational function $\boldsymbol{y}(s)$, where $\boldsymbol{y}_i := \boldsymbol{y}(z_i)$ for $i = 1, \ldots, N$, with $Y = \boldsymbol{y}_1, \ldots, \boldsymbol{y}_N$. By incorporating the left and right data partitions, the following expressions are obtained:

$$\begin{aligned} Z &= \left\{\lambda_1, \ldots, \lambda_\rho\right\} \cup \left\{\mu_1, \ldots, \mu_\nu\right\} \\ &\text{and} \\ Y &= \left\{\boldsymbol{w}_1, \ldots, \boldsymbol{w}_\rho\right\} \cup \left\{\boldsymbol{v}_1, \ldots, \boldsymbol{v}_\nu\right\}, \end{aligned} \tag{8}$$

where $N = p + \nu$. Consequently, the matrix $\mathbb{L}$ is presented as follows:

$$\mathbb{L} = \begin{bmatrix} \dfrac{\boldsymbol{v}_1\boldsymbol{r}_1 - \boldsymbol{l}_1\boldsymbol{w}_1}{\mu_1 - \lambda_1} & \cdots & \dfrac{\boldsymbol{v}_1\boldsymbol{r}\rho - \boldsymbol{l}_1\boldsymbol{w}\rho}{\mu_1 - \lambda\rho} \\ \vdots & \ddots & \vdots \\ \dfrac{\boldsymbol{v}_\nu\boldsymbol{r}_1 - \boldsymbol{l}_\nu\boldsymbol{w}_1}{\mu_\nu - \lambda_1} & \cdots & \dfrac{\boldsymbol{v}_\nu\boldsymbol{r}\rho - \boldsymbol{l}_\nu\boldsymbol{w}\rho}{\mu_\nu - \lambda\rho} \end{bmatrix} \in \mathbb{C}^{\nu\times\rho}. \tag{9}$$

As $\boldsymbol{v}_\nu\boldsymbol{r}_p$ and $\boldsymbol{l}_\nu\boldsymbol{w}_p$ are scalars, the Sylvester equation for $\mathbb{L}$ is satisfied in the following manner:

$$\mathbb{L}\boldsymbol{\Lambda} - \boldsymbol{M}\mathbb{L} = \boldsymbol{L}\boldsymbol{W} - \boldsymbol{V}\boldsymbol{R}. \tag{10}$$

The shifted Loewner matrix, $\mathbb{L}_{\mathrm{s}}$, is defined as the matrix $\mathbb{L}$ corresponding to $s\boldsymbol{H}(s)$:

$$\mathbb{L}_{\mathrm{s}} = \begin{bmatrix} \dfrac{\mu_1\boldsymbol{v}_1\boldsymbol{r}_1 - \lambda_1\boldsymbol{l}_1\boldsymbol{w}_1}{\mu_1 - \lambda_1} & \cdots & \dfrac{\mu_1\boldsymbol{v}_1\boldsymbol{r}_\rho - \lambda_\rho\boldsymbol{l}_1\boldsymbol{w}_\rho}{\mu_1 - \lambda_\rho} \\ \vdots & \ddots & \vdots \\ \dfrac{\mu_\nu\boldsymbol{v}_\nu\boldsymbol{r}_1 - \lambda_1\boldsymbol{l}_\nu\boldsymbol{w}_1}{\mu_\nu - \lambda_1} & \cdots & \dfrac{\boldsymbol{v}_\nu\boldsymbol{r}_\rho - \boldsymbol{l}_\nu\boldsymbol{w}_\rho}{\mu_\nu - \lambda_\rho} \end{bmatrix} \in \mathbb{C}^{\nu\times\rho}. \tag{11}$$

Similarly, the Sylvester equation is satisfied as follows:

$$\mathbb{L}_{\mathrm{s}}\boldsymbol{\Lambda} - \boldsymbol{M}\mathbb{L}_{\mathrm{s}} = \boldsymbol{L}\boldsymbol{W}\boldsymbol{\Lambda} - \boldsymbol{M}\boldsymbol{V}\boldsymbol{R}. \tag{12}$$

Without loss of generality, $\boldsymbol{D}$ can be considered 0, as its contribution does not influence the tangential interpolation of the LF [39]. For ease of presentation, the remainder of the discussion will focus on $\boldsymbol{H}(s)$. Consequently, Equation (4) simplifies to the following:

$$\boldsymbol{H}(s) = \boldsymbol{C}(s\boldsymbol{E} - \boldsymbol{A})^{-1}\boldsymbol{B}. \tag{13}$$

A minimal-dimensional realization is achievable only when the system is fully controllable and observable. Under the assumption that the data are sampled from a system whose transfer function is described by Equation (13), the generalized tangential observability, $\mathcal{O}_\nu$, and generalized tangential controllability, $\mathcal{R}_\rho$, are defined in Reference [41], such that Equations (9) and (11) can be rewritten as follows:

$$\mathbb{L} = -\mathcal{O}_\nu \boldsymbol{E}\mathcal{R}_\rho, \quad \mathbb{L}_s = -\mathcal{O}_\nu \boldsymbol{A}\mathcal{R}_\rho. \tag{14}$$

Then, by defining the Loewner pencil as a regular pencil, such that $\mathrm{eig}((\mathbb{L}, \mathbb{L}_s)) \neq (\mu_i, \lambda_i)$:

$$\boldsymbol{E} = -\mathbb{L}, \quad \boldsymbol{A} = -\mathbb{L}_s, \quad \boldsymbol{B} = \boldsymbol{V}, \quad \boldsymbol{C} = \boldsymbol{W}. \tag{15}$$

As a result, the interpolating rational function is defined as follows:

$$\boldsymbol{H}(s) = \boldsymbol{W}(\mathbb{L}_s - s\mathbb{L})^{-1}\boldsymbol{V}. \tag{16}$$

The derivation provided is specific to the minimal data scenario, which is rarely encountered in practical applications. However, the LF framework can be extended to handle redundant data points effectively. To begin, assume the following:

$$\begin{gathered}\mathrm{rank}\left[\zeta\mathbb{L} - \mathbb{L}_s\right] = \mathrm{rank}\left[\mathbb{L}\mathbb{L}_s\right] = \mathrm{rank}\left[\mathbb{L}\mathbb{L}_s\right] = k, \\ \forall\, \zeta \in \left\{\lambda_j\right\} \cup \left\{\mu_i\right\}.\end{gathered} \tag{17}$$

Next, the short Singular Value Decomposition (SVD) of $\zeta\mathbb{L} - \mathbb{L}_s$ is performed:

$$\mathrm{svd}\,(\zeta\mathbb{L} - \mathbb{L}_s) = \boldsymbol{Y}\boldsymbol{\Sigma}_l\boldsymbol{X}, \tag{18}$$

where $\mathrm{rank}(\zeta\mathbb{L} - \mathbb{L}_s) = \mathrm{rank}(\boldsymbol{\Sigma}_l) = \mathrm{size}(\boldsymbol{\Sigma}_l) = k$, $\boldsymbol{Y} \in \mathbb{C}^{\nu\times k}$ and $\boldsymbol{X} \in \mathbb{C}^{k\times\rho}$. Observe that

$$\begin{aligned}-\boldsymbol{A}\boldsymbol{X} + \boldsymbol{E}\boldsymbol{X}\boldsymbol{\Sigma}_l &= \boldsymbol{Y}^*\mathbb{L}_s\boldsymbol{X}^*\boldsymbol{X} - \boldsymbol{Y}^*\mathbb{L}\boldsymbol{X}^*\boldsymbol{X}\boldsymbol{\Sigma}_l \\ &= \boldsymbol{Y}^*(\mathbb{L}_s - \mathbb{L}\boldsymbol{\Sigma}_l) = \boldsymbol{Y}^*\boldsymbol{V}\boldsymbol{R} = \boldsymbol{B}\boldsymbol{R}.\end{aligned} \tag{19}$$

Similarly, $-\boldsymbol{Y}\boldsymbol{A} + \boldsymbol{M}\boldsymbol{Y}\boldsymbol{E} = \boldsymbol{L}\boldsymbol{C}$, where $\boldsymbol{X}$ and $\boldsymbol{Y}$ represent the generalized controllability and observability matrices, respectively, for the system $\boldsymbol{\Sigma}$ with $\boldsymbol{D} = 0$. Once the right and left interpolation conditions are verified, the Loewner realization for redundant data is expressed as follows:

$$\boldsymbol{E} = -\boldsymbol{Y}^*\mathbb{L}\boldsymbol{X}, \quad \boldsymbol{A} = -\boldsymbol{Y}^*\mathbb{L}_s\boldsymbol{X}, \quad \boldsymbol{B} = \boldsymbol{Y}^*\boldsymbol{V}, \quad \boldsymbol{C} = \boldsymbol{W}\boldsymbol{X}. \tag{20}$$

The formulation in Equation (20), which represents the Loewner realization for redundant data, will be used throughout this study. For a comprehensive explanation of each step, readers are directed to References [38, 39], while the MATLAB implementation can be found in Reference [42]. Finally, the system modal parameters can be determined through eigenanalysis of the system matrices $\boldsymbol{A}$ and $\boldsymbol{C}$ in Equation (20).

2.2 | Natural Excitation Technique

The NExT is a method used to extract Impulse Response Functions (IRFs) of structures subjected to ambient excitation [30]. Originally applied to wind turbines [27, 28], this approach is particularly suited to scenarios where input forces, such as wind or traffic, cannot be directly measured. The NExT algorithm works under the principle that ambient excitations serve as random broadband inputs, effectively exciting the structure.

NExT requires that the ambient vibration responses (in terms of acceleration, velocity, or displacement time series) of the target structure are recorded over a sufficiently long period, to ensure stationarity of operating conditions, which is critical for accurate analysis. Ambient forces, including wind, traffic, or thermal effects, can be assumed to act as random broadband inputs, exciting multiple structural modes simultaneously and, thus, allowing to provide a comprehensive representation of the dynamic behavior. The cross-correlation functions of these response signals are then calculated, either in the time domain or through Cross-Spectral Density in the frequency domain [43]. These cross-correlations mimic free vibration response, enabling the identification of modal parameters via standard methods as though an impulse force had been applied. The assumption of stationary excitations ensures that statistical properties, such as mean and variance, remain constant, allowing the cross-correlation functions to accurately reflect a system dynamic response.

A distinguishing feature of NExT is its reliance on cross-correlation functions between output signals. For two signals $x(t)$ and $y(t)$ measured at different locations, the cross-correlation function is defined as follows:

$$R_{xy}(\tau) = \lim_{T\to\infty} \frac{1}{T}\int_0^T x(t)y(t+\tau)\,\mathrm{d}t, \tag{21}$$

$R_{xy}(\tau)$ represents the cross-correlation function, which quantifies the similarity between the signals $x(t)$ and $y(t)$ as a function of the time lag τ. Here, $x(t)$ is the time-dependent output signal measured at one location on the structure, and $y(t)$ is the corresponding signal measured at a different location. The parameter τ denotes the time lag (or shift) between the two signals. The integration is performed over a time window of duration T, where T approaches infinity to ensure statistical accuracy. This function replicates the system IRF, enabling modal identification without requiring direct input measurements.

Thus, the idea in this study is to implement NExT on output-only vibration time series, obtain the system approximated IRF, convert it into the frequency domain (using the Fast Fourier Transform, implemented in MATLAB `fft` function[1]), and, finally, feed the FRF, that is, the frequency domain counterpart of the IRF, to the LF. On the other hand, only the IRF is needed for ERA, which is not explicitly discussed in this study as it is used solely as a benchmark method. The interested reader is referred to Reference [15] for a detailed overview of the method. The NExT and ERA implementations used in this study are retrieved from Reference [44].

3 | Numerical Case Study

To validate the proposed output-only modal identification method, a numerical system of an Euler–Bernoulli cantilever beam is introduced in Figure 1. The beam is divided into eight elements, with the constrained end located at node 0. The beam is made out of aluminum with a density (ρ) of 2700 kg m^{-3}, Young's modulus (E) of 70 GPa, and the cross-sectional parameters resulting from the dimensions in Figure 1. Modal damping ratio values of 1% and 3% are considered for all modes, and the mass and stiffness matrices are assembled from standard two-dimensional Euler–Bernoulli beam theory elements (see Equations A1 and A2 in Appendix A). This allows us to study the influence of ζ_n and noise on the identification accuracy by having two numerical models; by having two numerical models; one for relatively low ($\zeta_n = 1\%$) and the other for relatively high damping ($\zeta_n = 3\%$).

The numerical system is excited with a vertical force of unity, 1 N, at node 1 at the initial time $t = 0$ s. The response of the system is then recorded for 30 s at a sampling frequency, f_s, of 1800 Hz. The selected f_s allows the inspection of all modes below 900 Hz (Nyquist criterion), which in this case are eight. The modes peaks and phase shifts are clearly shown in Figure 2.

The baseline analytical modal data are obtained by eigenanalysis of the system mass and stiffness matrices and considering the imposed damping ratio. On the other hand, all the time history responses (eight displacement-only degrees of freedom) of the system are used to compute the system IRF via NExT, using the displacement response measured at node 1 as a reference channel. At that point, the IRF is used as input for ERA (NExT-ERA) and converted to the frequency domain to be used with LF (NExT-LF). On the other hand, the displacement time series is directly fed to SSI. The identification process is carried out over a range of orders ($k = [16\,100]$), and stabilization diagrams are used to extract the stable—likely physically meaningful—modes. These are not included here for brevity. The results, in terms of ω_n, ζ_n, and $\boldsymbol{\phi}_n$, are presented in Table 1 for the $\zeta_n = 1\%$ model and in Table 2 for $\zeta_n = 3\%$. The $\boldsymbol{\phi}_n$ identification results are presented using the Modal Assurance Criterion (MAC) value w.r.t. the analytical values. This data set does not address closely spaced—in frequency—modes as the LF has already been shown to outperform established methods in this regard, for example, least-squares complex exponential on a numerical system [25] and SSI and numerical algorithm for (4) subspace state space System IDentification on a full aircraft [35].

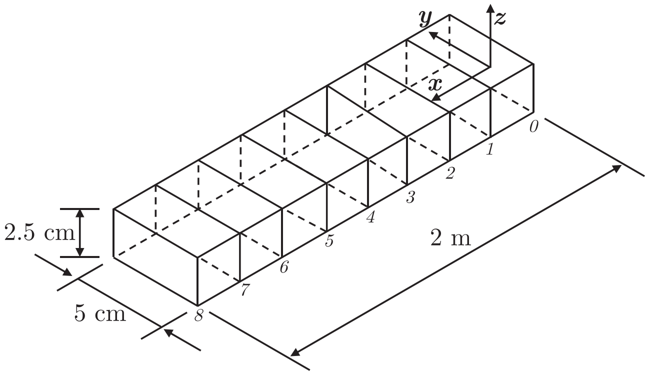

FIGURE 1 | Numerical case study: three-dimensional Euler–Bernoulli beam numerical system.

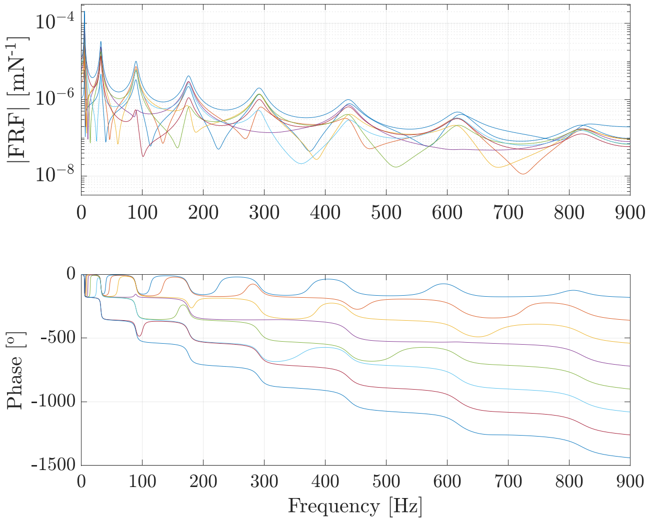

FIGURE 2 | Numerical case study: frequency response function (FRF) of the numerical system.

The values identified via NExT-LF, NExT-ERA, and SSI are widely coherent with those from the expected analytical values. In terms of ω_n, the largest deviation, in percentage, is 0.06% for all methods for modes #2 and #3 of the $\zeta_n = 3\%$ model. Concerning ζ_n, both methods show a great agreement with the numerical results (deviation ~0%), except for one case of NExT-ERA (ζ_1 for $\zeta_n = 3\%$, where the deviation is quite noticeable at −6.67%). Finally, the identified $\boldsymbol{\phi}_n$ MAC values are all close to 1 for both methods. However, this does not hold for the NExT-ERA identified $\boldsymbol{\phi}_8$ in the $\zeta_n = 3\%$ model, which is only 0.67; hence, not showing an appropriate correlation with the numerical counterpart. Thus, it can be said that the NExT-LF identification is more robust than NExT-ERA and shows a similar performance to SSI on unperturbed systems.

However, as per the definition, OMA is often adversely affected by environmental conditions, which in a signal can usually be modeled as noise. Consequently, to assess the newly proposed NExT-LF OMA suitability, the displacement response time series and input force of the two systems are corrupted with different levels of additive white Gaussian noise. The level is defined w.r.t. the standard deviation of the signal.[2] In this study, levels of 0.1%, 0.5%, 1%, 1.5%, and 2% are considered. The same identification process described above is carried out for the five resulting noise cases, and the results, in terms of deviation from the analytical results, for ω_n and ζ_n, and MAC values, for $\boldsymbol{\phi}_n$, are presented in Figures 3 and 4 for the $\zeta_n = 1\%$ and $\zeta_n = 3\%$ models, respectively. Please note that only the NExT-LF results are presented in Figure 4 for the $\zeta_n = 3\%$ model, as results similar to those for $\zeta_n = 1\%$ model (Figure 4) were found for NExT-ERA and SSI.

Figure 3A,D,G shows the difference in percentage (Δ) between the analytical and identified, respectively, via NExT-LF, NExT-ERA, and SSI, ω_n of the $\zeta_n = 0.1\%$ model. It is clear that, while all methods can deliver a full identification for the lowest noise case, the NExT-LF identification is much more robust to noise than that from NExT-ERA, both in terms of the number of modes identified and their accuracy. The same is shown in Figure 3B,E,H for ζ_n, but the NExT-LF identified modes with a NExT-ERA counterpart tend to show a slightly higher error,

TABLE 1 | Numerical (ζ_n = 1%) case study: Beam analytical and identified ω_n and ζ_n, and MAC values between the identified $\boldsymbol{\phi}_n$ and the analytical counterpart. In brackets is the percentage difference between the identified values and the analytical results.

$\zeta_n = 1\%$	Natural frequencies (Hz)				Damping ratio (—)			MAC (diagonal) value (—)		
Mode #	**Analytical**	**SSI**	**NExT-ERA**	**NExT-LF**	**SSI**	**NExT-ERA**	**NExT-LF**	**SSI**	**NExT-ERA**	**NExT-LF**
1	5.10	5.10	5.10	5.10	0.010	0.010	0.010	1	1	1
	—	(0.00)	(0.00)	(0.00)	(0.00)	(0.00)	(0.00)	—	—	—
2	31.97	31.99	31.99	31.99	0.010	0.010	0.010	1	1	1
	—	(0.01)	(0.01)	(0.01)	(0.00)	(0.00)	(0.00)	—	—	—
3	89.61	89.62	89.62	89.62	0.010	0.010	0.010	1	1	1
	—	(0.01)	(0.01)	(0.01)	(0.00)	(0.00)	(0.00)	—	—	—
4	175.89	175.90	175.90	175.90	0.010	0.010	0.010	1	1	1
	—	(0.01)	(0.01)	(0.01)	(0.00)	(0.00)	(0.00)	—	—	—
5	291.78	291.80	291.80	291.80	0.010	0.010	0.010	1	1	1
	—	(0.01)	(0.01)	(0.01)	(0.00)	(0.00)	(0.00)	—	—	—
6	438.52	438.54	438.54	438.54	0.010	0.010	0.010	1	1	1
	—	(0.01)	(0.01)	(0.01)	(0.00)	(0.00)	(0.00)	—	—	—
7	617.31	617.34	617.34	617.34	0.010	0.010	0.010	1	1	1
	—	(0.01)	(0.01)	(0.01)	(0.00)	(0.00)	(0.00)	—	—	—
8	820.08	820.12	820.12	820.12	0.010	0.010	0.010	1	1	1
	—	(0.01)	(0.01)	(0.01)	(0.00)	(0.00)	(0.00)	—	—	—

Abbreviations: ERA, Eigensystem Realization Algorithm; LF, Loewner Framework; MAC, Modal Assurance Criterion; NExT, Natural Excitation Technique; SSI, stochastic subspace identification.

TABLE 2 | Numerical case study: Beam analytical (3%) and identified ω_n and ζ_n, and MAC values between the identified $\boldsymbol{\phi}_n$ and the analytical counterpart. In brackets is the percentage difference between the identified values and the analytical results.

$\zeta_n = 3\%$	Natural frequencies (Hz)				Damping ratio (—)			MAC (diagonal) value (—)		
Mode #	**Analytical**	**SSI**	**NExT-ERA**	**NExT-LF**	**SSI**	**NExT-ERA**	**NExT-LF**	**SSI**	**NExT-ERA**	**NExT-LF**
1	5.10	5.10	5.10	5.10	0.030	0.028	0.030	1	1	1
	—	(0.00)	(0.00)	(0.00)	(0.00)	(−6.67)	(0.00)	—	—	—
2	31.97	31.99	31.99	31.99	0.030	0.030	0.030	1	1	1
	—	(0.06)	(0.06)	(0.06)	(0.00)	(0.00)	(0.00)	—	—	—
3	89.57	89.62	89.62	89.62	0.030	0.030	0.030	1	1	1
	—	(0.06)	(0.06)	(0.06)	(0.00)	(0.00)	(0.00)	—	—	—
4	175.82	175.90	175.90	175.90	0.030	0.030	0.030	1	1	1
	—	(0.05)	(0.05)	(0.05)	(0.00)	(0.00)	(0.00)	—	—	—
5	291.67	291.80	291.80	291.80	0.030	0.030	0.030	1	1	0.99
	—	(0.04)	(0.04)	(0.04)	(0.00)	(0.00)	(0.00)	—	—	—
6	438.34	438.54	438.54	438.54	0.030	0.030	0.030	1	1	0.99
	—	(0.05)	(0.05)	(0.05)	(0.00)	(0.00)	(0.00)	—	—	—
7	617.06	617.34	617.24	617.34	0.030	0.030	0.030	1	0.94	0.97
	—	(0.05)	(0.03)	(0.05)	(0.00)	(0.00)	(0.00)	—	—	—
8	819.75	820.12	820.12	820.12	0.030	0.030	0.030	1	0.65	0.90
	—	(0.05)	(0.05)	(0.05)	(0.00)	(0.00)	(0.00)	—	—	—

Abbreviations: ERA, Eigensystem Realization Algorithm; LF, Loewner Framework; MAC, Modal Assurance Criterion; NExT, Natural Excitation Technique; SSI, stochastic subspace identification.

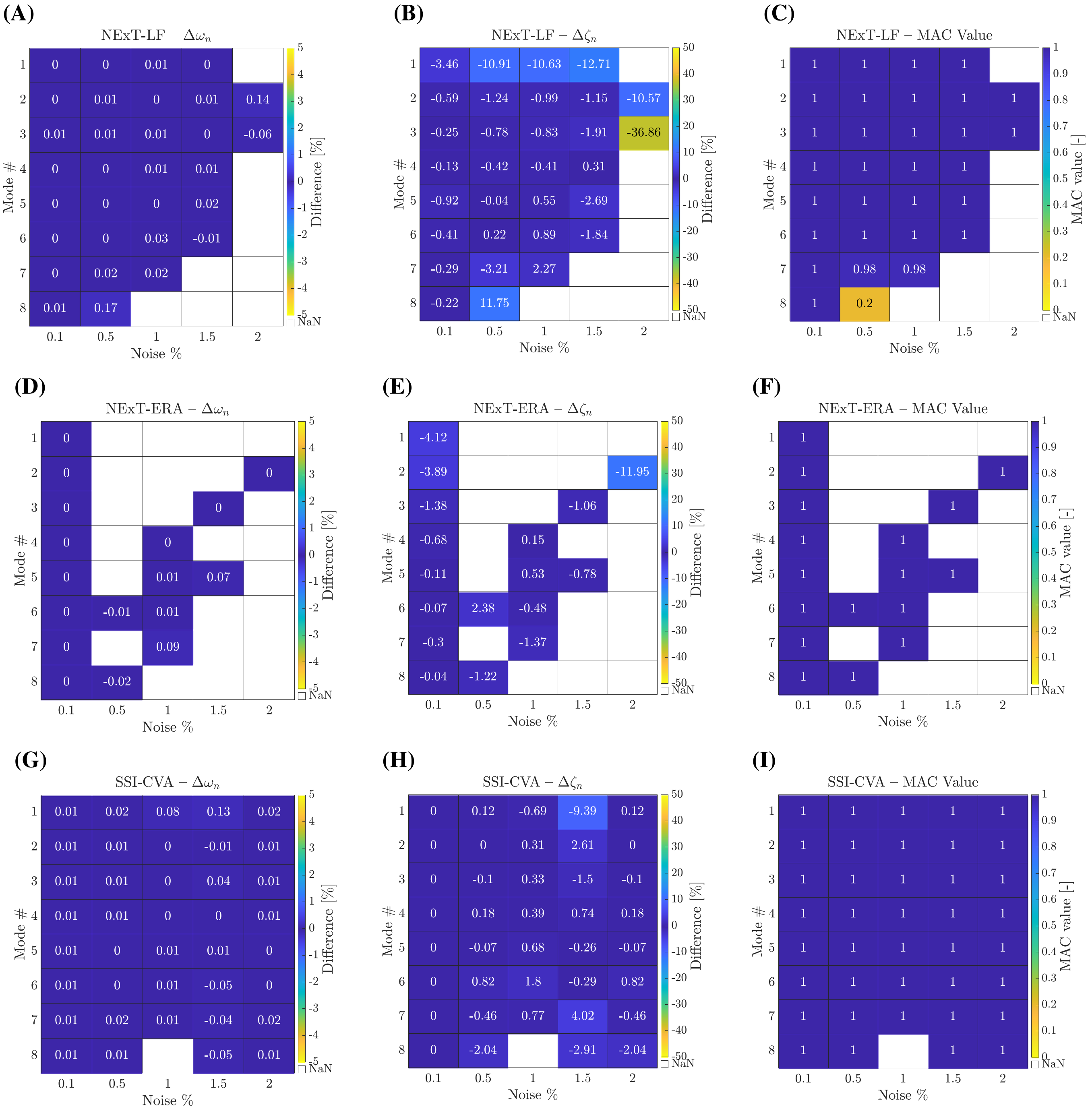

FIGURE 3 | Numerical ($\zeta_n = 1\%$) case study: Effects of input–output noise on the NExT-LF (top row - A to C), NExT-ERA (middle row - D to F), and SSI (bottom row - G to I) identifications (difference w.r.t. analytical results) of ω_n (A, D, G), ζ_n (B, E, H), and $\boldsymbol{\phi}_n$, expressed in terms of MAC value (C, F, I). CVA, canonical variate analysis; ERA, Eigensystem Realization Algorithm; LF, Loewner Framework; MAC, Modal Assurance Criterion; NExT, Natural Excitation Technique; SSI, stochastic subspace identification.

such as for modes #3 and #4 for the 0.5% noise case, which, however, is still well below 1%. Finally, the MAC values in Figure 3C,F,H, respectively, from the NExT-LF, NExt-ERA, and SSI identified $\boldsymbol{\phi}_n$, show that all modes identified via NExT-LF are well correlated with the numerical values, showing a minimum MAC value of 0.9. The same cannot be said for NExT-ERA, as the MAC value of $\boldsymbol{\phi}_8$ for the 0.1% case shows a value of 0.65. Nevertheless, SSI can identify all the modal parameters accurately at all noise levels, except for mode #8 at 1% noise, but NExT-LF still performs much better than NExT-ERA. Furthermore, a similar situation is found for the $\zeta_n = 0.3\%$ model, showing that damping does not affect the identification quality in noisy scenarios. This is supported by Figure 4, which is very similar to Figure 3A–C. The only difference is that the identification of mode #8 at 0.5% noise is lost, but mode #1 at 2% noise is gained.

Concluding on the numerical system, it can be asserted that NExT-LF performance, both in terms of accuracy and robustness to artificially added measurement noise, is better than

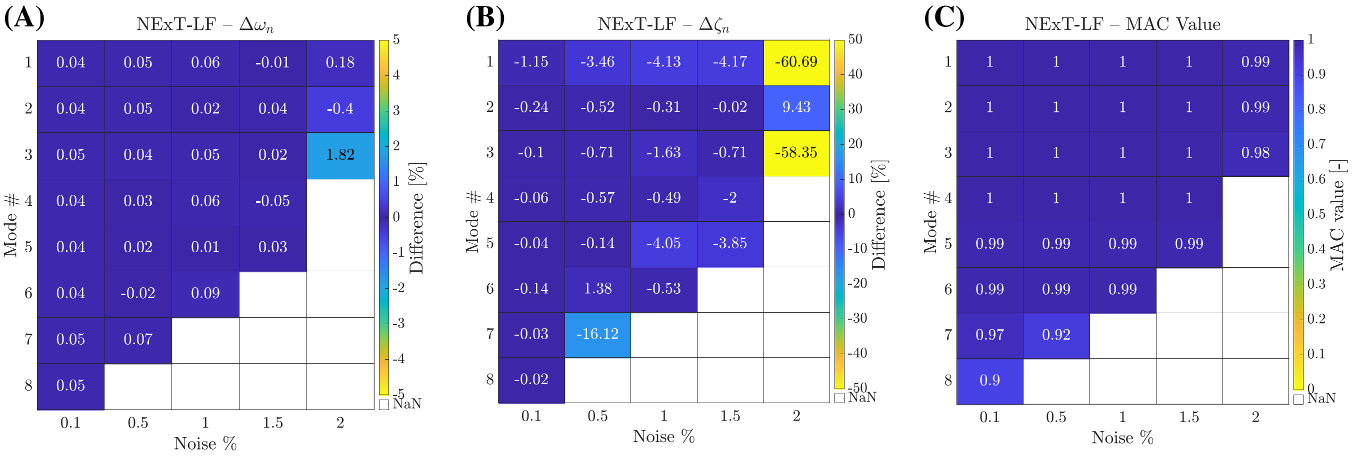

FIGURE 4 | Numerical ($\zeta_n = 3\%$) case study: Effects of input–output noise on the NExT-LF identification (difference w.r.t. analytical results) of ω_n (A), ζ_n (B), and $\boldsymbol{\phi}_n$—in terms of MAC value (C). LF, Loewner Framework; MAC, Modal Assurance Criterion; NExT, Natural Excitation Technique.

FIGURE 5 | Experimental case study: Sheraton Universal Hotel—Universal City, North Hollywood, California (USA)—in 1987. Location coordinates: 34°08′12. 0″ N, 118°21′36. 3″ W. Reproduced (adapted) under terms of the CC-BY license. Reference not available. Copyright 2016, the authors, published by Flickr Inc.

NExT-ERA. This is validated further on an experimental system in the following section.

4 | OMA of the Sheraton Universal Hotel

After the successful validation of the NExT-LF method on the numerical data set, a real-life and -size experimental case study is sought. This is found in the Sheraton Universal Hotel data set, which, despite some reported works for low-cycle damage fatigue and base shear estimation [45–47], does not, to this date and to the best of the authors' knowledge, include any results related to modal parameter identification in the current literature. Thus, this study aims to identify them with the newly proposed NExT-LF and the benchmark method, NExT-ERA.

The building, constructed in 1967 and shown in Figure 5, stands 173 ft and 3 in (54 m) tall. It has a rectangular plan with base dimensions of 96′4″ × 198′7″ (29.4 m × 60.5 m) and typical upper floor dimensions of 57′10″ × 183′6″ (17.6 m × 56 m). The vertical load system comprises 4.5–6 in (11.4–15.2 cm) thick concrete slabs supported by reinforced beams and columns, while ductile moment-resisting frames resist lateral forces. Spread footings form the foundation of the structure. The building has been permanently instrumented since the late 90s as part of the California Strong Motion Instrumentation Program with accelerometers installed across five floors [48].

Ambient vibration tests were conducted on December 18, 1997, by a team from the University of California, Irvine, Stanford University, and Los Alamos National Laboratory [49]. During the ambient vibration tests, excitation was primarily caused by environmental factors such as wind, traffic, and internal mechanical systems. Thirteen kinematrics accelerometers were used in conjunction with a Hewlett-Packard 3566A dynamic data acquisition system, enabling the recording and processing of signals. This setup included multiple modules for analog-to-digital conversion and signal processing.

The accelerometers were distributed across the building, as shown in Figure 6, to capture acceleration responses. Sensor positions were based on optimized coverage to assess the structural behavior effectively. Sampling parameters varied by test designation, with signals categorized into groups based on record length and f_s. Table 3 summarizes the test details.

The tests also incorporated velocity and displacement measurements from Kinemetrics Ranger Seismometers deployed at specific floors and directions. However, accelerometer-only signals are considered in this study. As shown in Figure 6, the basement excluded, there are 12 sensors located on the 3rd, 9th, and 16th floors, as well as on the roof. On each floor, two sensors are oriented North–South (positive direction toward the North) and one sensor perpendicularly (East–West, positive direction toward the East). With this sensor layout, the system can be identified using the recorded acceleration at these four instrumented floors only, as no additional degrees of freedom are available.

Considering a global coordinate system with the origin at the Southwest corner of the building, the y-axis points North, the x-axis points East, and the z-axis represents the elevation. The recorded signals are organized in a $12 \times N$ (N is the mode number) matrix, where

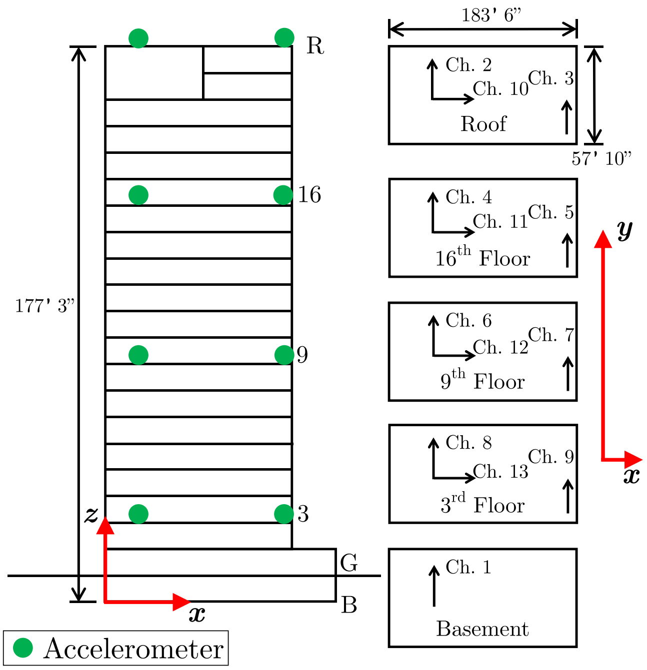

FIGURE 6 | Experimental case study: Location and direction of the sensors in the building. Green circles outline the accelerometer positions.

TABLE 3 | Experimental case study: Sampling parameters and signal length of the ambient vibration tests.

Test name	f_s (Hz)	Record length (s)
SH158	32	64
SH258	32	64
SH358	16	256
SH458	16	256
SH558	16	512
SH658	16	512

- The first four rows represent acceleration in the y-direction.
- The next four rows represent acceleration in the x-direction.
- The final four rows represent rotational signals for each floor, calculated as the difference between two sensors in the y-direction, multiplied by their distance.

For visualization purposes, the FRF derived from the NExT-derived IRF for reference channel five from test case SH258 is shown in Figure 7.

4.1 | Results

Initially, unprocessed signal data were analyzed, revealing significant noise interference. To address this, two filters were applied: a bandpass filter for the range of 0.4–9.5 Hz and an empirical Bayesian method with a Cauchy prior. These were implemented in MATLAB using the built-in functions `bandpass`[3] and `wdenoise`,[4] respectively.

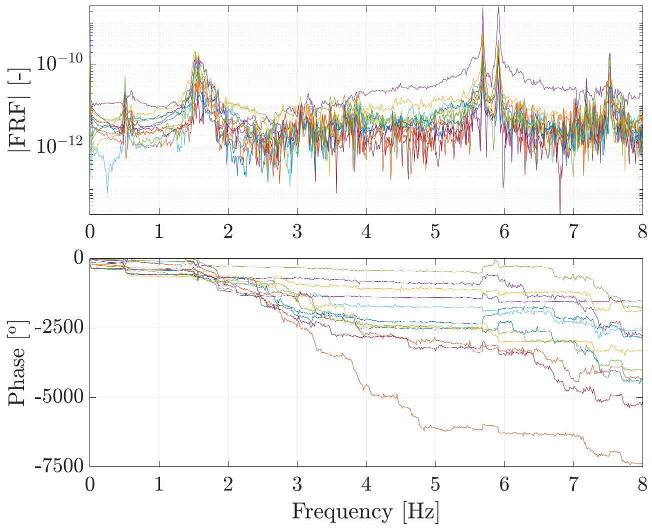

FIGURE 7 | Experimental case study: Unfiltered frequency response function (FRF) of the Sheraton Universal Hotel as computed from the NExT-derived IRF for reference channel 5 and test case SH258. IRF, Impulse Response Function; NExT, Natural Excitation Technique.

The SI of the Sheraton Hotel was performed using both NExT-LF and NExT-ERA methods. All six data sets (SH158-SH658) were analyzed, with different reference channels applied in each analysis to explore all potential outcomes. By evaluating the unfiltered, bandpass filtered, and denoised signals across these data sets, as well as employing five different reference channels per data set, a total of 90 analyses were conducted. Despite the varying conditions across these analyses, the results for the low-frequency modes were largely consistent. In all instances, stabilization diagrams were used to identify the stable modes.

The NExT-LF and NExT-ERA identification of the signals revealed significant noise, which affected the stability of mode identification. Notably, NExT-ERA showed a recurring tendency to detect spurious modes, while NExT-LF identified fewer stable modes. However, the modes identified by NExT-LF consistently aligned with FRF peaks demonstrate superior robustness to noise. Thus, the results of this experimental data set are in agreement with those of the numerical system described in Section 3. This distinction highlights the effectiveness of NExT-LF in minimizing the detection of fictitious modes.

Using different reference channels resulted in slight variations in the identified modes. Reference channels aligned with the Y-direction (e.g., reference channel #5) tended to result in the identification of more modes. Low-frequency modes were consistently detected within a narrow frequency range across analyses, with examples such as the first mode appearing at 0.64 Hz in one analysis and 0.68 Hz in another, both exhibiting similar mode shapes and damping ratios.

Across all analyses, five stable modes were identified. These modes showed consistency in their natural frequencies (ω_n), damping ratios (ζ_n), and mode shapes ($\boldsymbol{\phi}_n$), and both NExT-LF and NExT-ERA methods detected them. These, featuring the full $\boldsymbol{\phi}_n$ results following this breakdown described above, are

TABLE 4 | Natural frequencies, damping ratios, and MAC values for modes identified using NExT-ERA and NExT-LF.

Mode #	Natural frequencies (Hz)		Damping ratio (—)		MAC value (—)
	NExT-ERA	NExT-LF	NExT-ERA	NExT-LF	NExT-ERA versus NExT-LF
1	0.64	0.64	0.02	0.03	1
2	1.86	1.86	0.02	0.01	1
3	3.40	3.40	0.02	0.02	0.99
4	6.02	6.01	0.02	0.02	0.93
5	7.00	6.99	0.01	0.01	0.99

Abbreviations: ERA, Eigensystem Realization Algorithm; LF, Loewner Framework; MAC, Modal Assurance Criterion; NExT, Natural Excitation Technique.

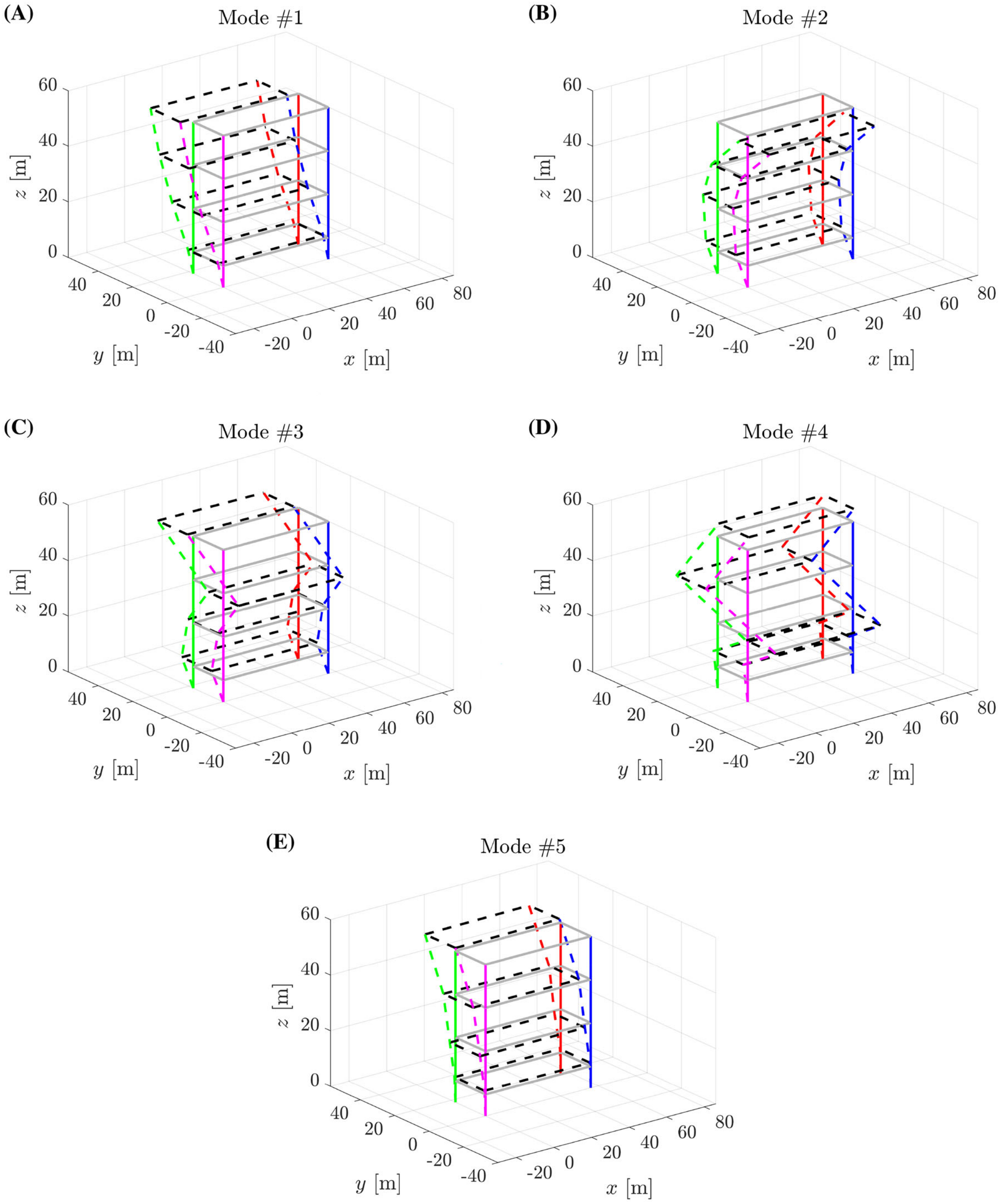

FIGURE 8 | Experimental case study: $\boldsymbol{\phi}_n$ of the Sheraton Universal Hotel's first five modes (in this order, from A to E) as identified via NExT-LF. LF, Loewner Framework; NExT, Natural Excitation Technique.

shown in Table B1 in Appendix B, while Table 4, here, shows the MAC value between the NExT-ERA and NExT-LF $\boldsymbol{\phi}_n$.

Furthermore, the identified $\boldsymbol{\phi}_n$ via NExT-LF is shown in Figure 8. Only those identified via NExT-LF are presented since the MAC values with the NExT-ERA identified modes are close to 1.

The $\boldsymbol{\phi}_n$ of the first five modes is consistent with what is expected from a shear-type building such as the one investigated here. Global mode #1 (0.64 Hz) is the first flexural mode, vibrating in a direction very close to the principal axis for which the moment of inertia is minimum. Probably due to mass and/or stiffness asymmetries in the building, this direction of vibration is not perfectly aligned with the axis along the shorter side of the rectangular plan view, and it is slightly skewed. Global modes #2, #3, and #4 (1.86, 3.49, and 6.01 Hz, respectively) are the second, third, and fourth flexural modes along the same direction. Finally, the last identified mode, global mode #5 (6.99 Hz), is the first bending mode in the (stiffer) orthogonal direction, which is, by contrast, occurring almost aligned with the other principal axis of inertia in the horizontal plane. No local modes were identified in the process; again, this is not particularly surprising due to the relatively simple and compact shape of the building, with no appendages, geometric irregularities in vertical or plan view, or soft storeys.

5 | Conclusions

This study introduced a novel OMA method, known as NExT-LF, that combines the NExT with the LF. The proposed method was validated through numerical and experimental case studies, demonstrating significant improvements in accuracy and robustness to noise compared to traditional methods, such as NExT-ERA (NExT with the ERA). The following conclusions can be drawn:

- NExT-LF identified stable modal parameters under varying noise conditions, outperforming NExT-ERA in terms of reliability, noise-robustness sense, and accuracy.
- The modal parameters identified from the numerical system showed minimal deviations from analytical values, with NExT-LF achieving a better alignment than NExT-ERA and similar performance to SSI to the expected analytical values.
- This study presented the first-ever modal parameter identification for the Sheraton Universal Hotel, successfully applying NExT-LF to a real-world operational scenario.

The proposed method offers a robust framework for OMA, with potential applications in SHM and operational identification of aeronautical systems, for example, wings in a wind tunnel test. Further validation will be sought from experimental case studies of output-only data with interesting closely spaced modes.

Author Contributions

Conceptualization: Gabriele Dessena and Marco Civera. Methodology: Gabriele Dessena, Marco Civera, and Ali Yousefi. Software: Gabriele Dessena and Ali Yousefi. Validation: Gabriele Dessena, Marco Civera, and Ali Yousefi. Formal analysis: Gabriele Dessena and Ali Yousefi. Investigation: Gabriele Dessena and Ali Yousefi. Resources: Gabriele Dessena and Marco Civera. Data curation: Gabriele Dessena, Marco Civera, and Ali Yousefi. Writing – original draft preparation: Gabriele Dessena and Marco Civera. Writing – review and editing: Gabriele Dessena, Marco Civera, and Cecilia Surace. Visualization: Gabriele Dessena, Marco Civera, and Ali Yousefi. Supervision: Gabriele Dessena, Marco Civera, and Cecilia Surace. Funding acquisition: Gabriele Dessena and Marco Civera.

Acknowledgments

The first author has been supported by the Madrid Government (Comunidad de Madrid—Spain) under the Multiannual Agreement with the Universidad Carlos III de Madrid (UC3M) (IA_aCTRl-CM-UC3M) and by the Grants for research activity of young PhD holders, part of the UC3M Own Research Program (Ayudas para la Actividad Investigadora de los Jóvenes Doctores, del Programa Propio de Investigación de la UC3M). The second author is supported by the Centro Nazionale per la Mobilità Sostenibile (MOST—Sustainable Mobility Center), Spoke 7 (Cooperative Connected and Automated Mobility and Smart Infrastructures), Work Package 4 (Resilience of Networks, Structural Health Monitoring and Asset Management). The authors thank the Center for Engineering Strong Motion Data (CESMD) for making the Sheraton Universal City Ambient Vibration Tests data set publicly available.

Conflicts of Interest

The authors declare no conflicts of interest.

Data Availability Statement

The data that support the findings of this study (Data supporting: NExT-LF: A Novel Operational Modal Analysis Method via Tangential Interpolation—Data file 1) are openly available in Zenodo at https://doi.org/10.5281/zenodo.14975925. In addition, this study used third-party experimental data (Sheraton Universal City Ambient Vibration Tests—Data file 2) that the authors do not have permission to share.[5] Data file 1 is available under the terms of the (GNU General Public License v3.0 [GPL 3.0]).

Endnotes

[1] See https://uk.mathworks.com/help/matlab/ref/fft.html.

[2] MATLAB notation: `signal+std(signal.*rand(size(size)*noise_level`, where `std` is found at https://uk.mathworks.com/help/matlab/ref/double.std.html and `rand` at https://uk.mathworks.com/help/matlab/ref/rand.html.

[3] See https://uk.mathworks.com/help/signal/ref/bandpass.html.

[4] See https://uk.mathworks.com/help/wavelet/ref/wdenoise.html.

[5] As of the writing of this article (December 11, 2024), the data set is not available anymore from the CESMD website. The data used in this study was retrieved on January 1, 2022.

References

1. G. Dessena, D. I. Ignatyev, J. F. Whidborne, A. Pontillo, and L. Zanotti Fragonara, "Ground Vibration Testing of a Flexible Wing: A Benchmark and Case Study," *Aerospace* 9, no. 8 (2022): 438, https://doi.org/10.3390/aerospace9080438.

2. T. Verhulst, D. Judt, C. Lawson, Y. Chung, O. Al-Tayawe, and G. Ward, "Review for State-of-the-Art Health Monitoring Technologies on Airframe Fuel Pumps," *International Journal of Prognostics and Health Management* 13, no. 1 (2022): 1–20, https://doi.org/10.36001/ijphm.2022.v13i1.3134.

3. M. Civera, G. Calamai, and L. Zanotti Fragonara, "System Identification via Fast Relaxed Vector Fitting for the Structural Health Monitoring

of Masonry Bridges," *Structures* 30, no. January (2021): 277–293, https://doi.org/10.1016/j.istruc.2020.12.073.

4. P. Lubrina, S. Giclais, C. Stephan, M. Boeswald, Y. Govers, and N. Botargues, "AIRBUS A350 XWB GVT: State-of-the-Art Techniques to Perform a Faster and Better GVT Campaign," in *Topics in Modal Analysis II, Volume 8. Conference Proceedings of the Society for Experimental Mechanics Series*, Vol. 45, ed. R. Allemang (Springer, Cham, 2014), 243–256, https://doi.org/10.1007/978-3-319-04774-4_24.

5. G. Dessena, D. I. Ignatyev, J. F. Whidborne, and L. Zanotti Fragonara, "A Global-Local Meta-Modelling Technique for Model Updating," *Computer Methods in Applied Mechanics and Engineering* 418, no. 6 (2024): 116511, https://doi.org/10.1016/j.cma.2023.116511.

6. A. Cadoret, E. Denimal-Goy, J. M. Leroy, J. L. Pfister, and L. Mevel, "Damage Detection and Localization Method for Wind Turbine Rotor Based on Operational Modal Analysis and Anisotropy Tracking," *Mechanical Systems and Signal Processing* 224, no. September 2024 (2025): 111982, https://doi.org/10.1016/j.ymssp.2024.111982.

7. C. R. Farrar, N. Dervilis, and K. Worden, "The Past, Present and Future of Structural Health Monitoring: An Overview of Three Ages," *Strain* 61, no. 1 (2025): e12495, https://doi.org/10.1111/str.12495.

8. K. Liu, E. Reynders, G. De Roeck, and G. Lombaert, "Experimental and Numerical Analysis of a Composite Bridge for High-Speed Trains," *Journal of Sound and Vibration* 320, no. 1–2 (2009): 201–220, https://doi.org/10.1016/j.jsv.2008.07.010.

9. B. Kavyashree, S. Patil, and V. S. Rao, "Review on Vibration Control in Tall Buildings: From the Perspective of Devices and Applications," *International Journal of Dynamics and Control* 9, no. 3 (2021): 1316–1331, https://doi.org/10.1007/s40435-020-00728-.

10. S. A. Bochkarev and S. V. Lekomtsev, "Analysis of Natural Vibration of Truncated Conical Shells Partially Filled With Fluid," *International Journal of Mechanical System Dynamics* 4, no. 2 (2024): 142–152, https://doi.org/10.1002/msd2.12105.

11. B. Li, W. Zhao, Y. Miao, W. Tian, and W. Liao, "A Method for Dynamic Parameter Identification of an Industrial Robot Based on Frequency Response Function," *International Journal of Mechanical System Dynamics* 4, May (2024): 461–471, https://doi.org/10.1002/msd2.12131.

12. L. Sibille, M. Civera, L. Zanotti Fragonara, and R. Ceravolo, "Automated Operational Modal Analysis of a Helicopter Blade With a Density-Based Cluster Algorithm," *AIAA Journal* 61, no. 3 (2023): 1411–1427, https://doi.org/10.2514/1.J062084.

13. G. S. Aglietti, M. Remedia, M. Appolloni, and A. Kiley, "Spacecraft Structure Model Validation and Test Philosophy," *AIAA Journal* 57, no. 5 (2019): 2109–2122, https://doi.org/10.2514/1.J057757.

14. B. Peeters and G. De Roeck, "One-Year Monitoring of the Z24-Bridge: Environmental Effects Versus Damage Events," *Earthquake Engineering & Structural Dynamics* 30, no. 2 (2001): 149–171, https://doi.org/10.1002/1096-9845(200102)30:2<149::AID-EQE1>3.0.CO;2-Z.

15. R. S. Pappa, G. H. James, and D. C. Zimmerman, "Autonomous Modal Identification of the Space Shuttle Tail Rudder," *Journal of Spacecraft and Rockets* 35, no. 2 (1998): 163–169, https://doi.org/10.2514/2.3324.

16. C. Gentile and A. Saisi, "Ambient Vibration Testing of Historic Masonry Towers for Structural Identification and Damage Assessment," *Construction and Building Materials* 21, no. 6 (2007): 1311–1321, https://doi.org/10.1016/j.conbuildmat.2006.01.007.

17. L. Ljung, T. Chen, and B. Mu, "A Shift in Paradigm for System Identification," *International Journal of Control* 93, no. 2 (2020): 173–180, https://doi.org/10.1080/00207179.2019.1578407.

18. E. Reynders, "System Identification Methods for (Operational) Modal Analysis: Review and Comparison," *Archives of Computational Methods in Engineering* 19, no. 1 (2012): 51–124, https://doi.org/10.1007/s11831-012-9069x.

19. V. Mugnaini, L. Zanotti Fragonara, and M. Civera, "A Machine Learning Approach for Automatic Operational Modal Analysis," *Mechanical Systems and Signal Processing* 170, no. February (2022): 108813, https://doi.org/10.1016/j.ymssp.2022.108813.

20. B. J. O'Connell and T. J. Rogers, "A Robust Probabilistic Approach to Stochastic Subspace Identification," *Journal of Sound and Vibration* 581, no. March (2024): 118381, https://doi.org/10.1016/j.jsv.2024.118381.

21. A. J. Elliott, A. Nakhaeezadeh Gutierrez, L. Felicetti, and L. Zanotti Fragonara, "In-Orbit System Identification of a Flexible Satellite With Variable Mass Using Dual Unscented Kalman Filters," *Acta Astronautica* 226, no. P2 (2025): 71–86, https://doi.org/10.1016/j.actaastro.2024.11.014.

22. Z. Zhu, S. K. Au, B. Li, and Y. L. Xie, "Bayesian Operational Modal Analysis With Multiple Setups and Multiple (Possibly Close) Modes," *Mechanical Systems and Signal Processing* 150 (2021): 107261, https://doi.org/10.1016/j.ymssp.2020.107261.

23. S. Grivet-Talocia and B. Gustavsen, *Passive Macromodeling: Theory and Applications* (Wiley, 2016).

24. M. Civera, G. Calamai, and L. Zanotti Fragonara, "Experimental Modal Analysis of Structural Systems by Using the Fast Relaxed Vector Fitting Method," *Structural Control and Health Monitoring* 28, no. 4 (2021): 1–23, https://doi.org/10.1002/stc.2695.

25. G. Dessena, M. Civera, L. Zanotti Fragonara, D. I. Ignatyev, and J. F. Whidborne, "A Loewner-Based System Identification and Structural Health Monitoring Approach for Mechanical Systems," *Structural Control and Health Monitoring* 2023 (2023): 1–22, https://doi.org/10.1155/2023/1891062.

26. S. Lefteriu and A. C. Antoulas, "Modeling Multi-Port Systems From Frequency Response Data via Tangential Interpolation," in *2009 IEEE Workshop on Signal Propagation on Interconnects* (IEEE, 2009), 1–4, https://doi.org/10.1109/SPI.2009.5089847.

27. T. Carne, J. Lauffer, A. J. Gomez, and H. Benjannet, "Modal Testing if a Very Flexible 110 m Wind Turbine Structure," in *Proceedings of the Sixth International Modal Analysis Conference (IMAC)* (Union College and Society of Experimental Mechanics, 1988).

28. J. P. Lauffer, T. G. Carne, and T. D. Ashwill, *Modal Testing in the Design Evaluation of Wind Turbines* (Sandia National Laboratories, 1988).

29. J. N. Juang and R. S. Pappa, "An Eigensystem Realization Algorithm in Frequency Domain for Modal Parameter Identification," *Journal of Guidance, Control, and Dynamics* 8, no. 5 (1986): 620–627, https://doi.org/10.2514/6.1986-2048.

30. G. H. James, III, T. G. Carne, and J. P. Lauffer, *The Natural Excitation Technique (NExT) for Modal Parameter Extraction From Operating Wind Turbines* (Sandia National Laboratories, 1993).

31. P. Van Overschee and B. De Moor, *Subspace Identification for Linear Systems* (Springer, 1996), https://doi.org/10.1007/978-1-4613-0465-4.

32. D. Quero, P. Vuillemin, and C. Poussot-Vassal, "A Generalized State-Space Aeroservoelastic Model Based on Tangential Interpolation," *Aerospace* 6, no. 1 (2019): 9, https://doi.org/10.3390/aerospace6010009.

33. G. Dessena, M. Civera, D. I. Ignatyev, J. F. Whidborne, L. Zanotti Fragonara, and B. Chiaia, "The Accuracy and Computational Efficiency of the Loewner Framework for the System Identification of Mechanical Systems," *Aerospace* 10, no. 6 (2023): 571, https://doi.org/10.3390/aerospace10060571.

34. G. Dessena, M. Civera, A. Pontillo, D. I. Ignatyev, J. F. Whidborne, and L. Zanotti Fragonara, "Noise-Robust Modal Parameter Identification and Damage Assessment for Aero-Structures," *Aircraft Engineering and Aerospace Technology* 96, no. 11 (2024): 27–36, https://doi.org/10.1108/AEAT-06-2024-0178.

35. G. Dessena and M. Civera, “Improved Tangential Interpolation-Based Multi-Input Multi-Output Modal Analysis of a Full Aircraft,” *European Journal of Mechanics—A/Solids* 110, no. March/April (2025): 105495, https://doi.org/10.1016/j.euromechsol.2024.105495.

36. G. Dessena, M. Civera, A. Marcos, and B. Chiaia, “Multi-Input Multi-Output Loewner Framework for Vibration-Based Damage Detection on a Trainer Jet,” *arXiv* (2024): 1–29, https://doi.org/10.48550/arXiv.2410.20160.

37. K. Löwner, “Über monotone matrixfunktionen,” *Mathematische Zeitschrift* 38, no. 1 (1934): 177–216, https://doi.org/10.1007/BF01170633.

38. A. C. Antoulas, S. Lefteriu, and A. C. Ionita, “A Tutorial Introduction to the Loewner Framework for Model Reduction,” in *Model Reduction and Approximation. No. May 2011* (Society for Industrial and Applied Mathematics, 2017), 335–376, https://doi.org/10.1137/1.9781611974829.ch8.

39. A. J. Mayo and A. C. Antoulas, “A Framework for the Solution of the Generalized Realization Problem,” *Linear Algebra and Its Applications* 425, no. 2/3 (2007): 634–662, https://doi.org/10.1016/j.laa.2007.03.008.

40. B. Kramer and S. Gugercin, “Tangential Interpolation-Based Eigensystem Realization Algorithm for MIMO Systems,” *Mathematical and Computer Modelling of Dynamical Systems* 22, no. 4 (2016): 282–306, https://doi.org/10.1080/13873954.2016.1198389.

41. S. Lefteriu and A. C. Antoulas, “A New Approach to Modeling Multiport Systems From Frequency-Domain Data,” *IEEE Transactions on Computer-Aided Design of Integrated Circuits and Systems* 29, no. 1 (2010): 14–27, https://doi.org/10.1109/TCAD.2009.2034500.

42. G. Dessena, *A Tutorial on the Loewner-Based System Identification and Structural Health Monitoring Approach for Mechanical Systems* (Cranfield University, 2023), https://doi.org/10.17862/cranfield.rd.16636279.

43. J. S. Bendat and A. G. Piersol, *Engineering Applications of Correlation and Spectral Analysis* (Wiley, 2013), 2nd ed.

44. A. Al-Rumaithi, *Eigensystem Realization Algorithm (ERA)* (2024), accessed September 3, 2023, https://www.mathworks.com/matlabcentral/fileexchange/69494-eigensystem-realization-algorithm-era.

45. R. K. Goel, “Challenges in Base Shear Estimation From Recorded Motions,” in *Structures Congress 2010* (American Society of Civil Engineers, 2010), 3207–3215, https://doi.org/10.1061/41130%28369%29288.

46. R. K. Goel, “Limitations of Estimating Base Shear Demand in Existing Building From Recorded Motions,” in *9th US National and 10th Canadian Conference on Earthquake Engineering 2010, Including Papers From the 4th International Tsunami Symposium*, Vol. 9 no. 164 (Canadian Association for Earthquake Engineering and Seismology, 2010).

47. A. Mantawy and J. Anderson, “Assessment of Low-Cycle Fatigue Damage in R.C. Frame Buildings Under Long-Duration Earthquakes,” in *SECED 2015 Conference: Earthquake Risk and Engineering towards a Resilient World* (Society for Earthquake and Civil Engineering Dynamics, 2015).

48. Center for Engineering Strong Motion Data (CESMD), North Hollywood—20-Story Hotel, accessed January 1, 2022, https://www.strongmotioncenter.org/cgi-bin/CESMD/stationhtml.pl?stationID=CE24464&network=CGS.

49. Center for Engineering Strong Motion Data (CESMD), Sheraton Universal City Ambient Vibration Tests (1997), accessed January 1, 2022, https://www.strongmotioncenter.org/cgi-bin/CESMD/Multiplesearch1_DM2.pl?event_name=&magmin=&magmax=&byear=&eyear=&country=Any&state=Any&stn_ident=&network=CE&sta_number=24464&type=Any&Material=Any&Height=&siteclass=Any&accmin=&accmax=&hdistmin=&hdistmax=.

Appendix A

Beam Element Matrices

The Euler–Bernoulli beam element mass and stiffness matrices are presented, respectively, in Equations (A1) and (A2).

$$\boldsymbol{M}_{\mathrm{e}} = \frac{\rho A L}{420}\begin{bmatrix} 156 & 22L & 54 & -13L \\ 22L & 4L^2 & 13L & -3L^2 \\ 54 & 13L & 156 & -22L \\ -13L & -3L^2 & -22L & 4L^2 \end{bmatrix}, \tag{A1}$$

$$\boldsymbol{K}_{\mathrm{e}} = \frac{EI}{L^3}\begin{bmatrix} 12 & 6L & -12 & 6L \\ 6L & 4L^2 & -6L & 2L^2 \\ -12 & -6L & 12 & -6L \\ 6L & 2L^2 & -6L & 4L^2 \end{bmatrix}, \tag{A2}$$

where ρ is the material density, A is the cross-sectional area, L is the element length, and EI is the bending stiffness (Young's modulus × second moment of area).

Appendix B

Sheraton Universal Hotel Raw Identification Results

The raw identification results of the Sheraton Universal Hotel are shown in Table B1.

TABLE B1 | Modal parameters of Sheraton Universal Hotel identified using NExT-ERA and NExT-LF.

	Mode #1		Mode #2		Mode #3		Mode #4		Mode #5	
Parameter	**NExT-ERA**	**NExT-LF**	**NExT-ERA**	**NExT-LF**	**NExT-ERA**	**NExT-LF**	**NExT-ERA**	**NExT-LF**	**NExT-ERA**	**NExT-LF**
ω_n (Hz)	0.64	0.64	1.86	1.86	3.40	3.40	6.02	6.01	7.00	6.99
ζ_n (—)	0.02	0.03	0.02	0.01	0.02	0.02	0.02	0.02	0.01	0.01
$\boldsymbol{\phi}_n$ ($y3$)	0	0	0.02	0.01	0.01	0.03	1	−0.66	0.11	0.16
$\boldsymbol{\phi}_n$ ($y9$)	−0.01	−0.01	0.03	0.02	0.01	0.02	−0.95	1	−0.05	−0.14
$\boldsymbol{\phi}_n$ ($y16$)	−0.01	−0.02	0	0	−0.02	−0.04	0.83	−0.62	0.06	0.14
$\boldsymbol{\phi}_n$ (yR)	−0.02	−0.02	−0.04	−0.04	0.04	0.06	0.07	−0.5	1	1
$\boldsymbol{\phi}_n$ ($x3$)	0	0	0.01	0	0	0	0.37	−0.5	0.09	0.11
$\boldsymbol{\phi}_n$ ($x9$)	0	0	0.02	−0.01	0	0	−0.05	0.16	−0.26	−0.27
$\boldsymbol{\phi}_n$ ($x16$)	0	0	0	0	0.01	0	−0.36	0.53	−0.16	−0.2
$\boldsymbol{\phi}_n$ (xR)	0	0	−0.02	0.01	0	0	0.43	−0.48	0.06	0.11
$\boldsymbol{\phi}_n$ ($r3$)	0.07	0.13	−0.35	−0.37	−0.7	−0.74	−0.02	0.01	0	−0.01
$\boldsymbol{\phi}_n$ ($r9$)	0.42	0.42	−0.89	−0.94	−0.11	−0.31	0.02	−0.02	0	0.01
$\boldsymbol{\phi}_n$ ($r16$)	0.75	0.66	−0.13	−0.24	1	1	−0.02	0.01	0.01	−0.01
$\boldsymbol{\phi}_n$ (rR)	1	1	−0.89	−0.77	0	0	0	0	0.02	0.03

Abbreviations: ERA, Eigensystem Realization Algorithm; LF, Loewner Framework; NExT, Natural Excitation Technique.